

Gamma-ray bursts from internal shocks in a relativistic wind : an hydrodynamical study.

F. Daigne* and R. Mochkovitch

Institut d'Astrophysique de Paris, CNRS, 98 bis Boulevard Arago, 75014 Paris, France

Received **.**.** / Accepted **.**.**

Abstract. The internal shock model for gamma-ray bursts involves shocks taking place in a relativistic wind with a very inhomogeneous initial distribution of the Lorentz factor. We have developed a 1D lagrangian hydrocode to follow the evolution of such a wind and the results we have obtained are compared to those of a simpler model presented in a recent paper (Daigne & Mochkovitch 1998) where all pressure waves are suppressed in the wind so that shells with different velocities only interact by direct collisions. The detailed hydrodynamical calculation essentially confirms the conclusion of the simple model: the main temporal and spectral properties of gamma-ray bursts can be reproduced by internal shocks in a relativistic wind.

Key words: Gamma rays: bursts – Hydrodynamics – Shock waves – Relativity – Radiation mechanisms: non-thermal

1. Introduction

Since the discovery of the optical counterpart of GRB 970228 (van Paradijs et al. 1997) the accurate localizations provided by the *Beppo-SAX* satellite have led to the detection of the optical afterglow for more than ten gamma-ray bursts (hereafter GRBs). The most spectacular result of these observations is to have provided a direct proof of the cosmological origin of GRBs. The detection of absorption lines at $z = 0.835$ in the spectrum of GRB 970508 (Metzger et al. 1997) followed by other redshift determinations (between $z = 0.43$ and $z = 3.41$) confirmed the indications which were already available from the *BATSE* data showing a GRB distribution perfectly isotropic but non homogeneous in distance (Fishman and Meegan 1995 and references therein).

The energy release of GRBs with known redshifts extends from $E_\gamma = 2 \cdot 10^{51} \frac{\Omega}{4\pi}$ to $E_\gamma = 2 \cdot 10^{54} \frac{\Omega}{4\pi}$ erg. The

solid angle Ω in which the emission is beamed is quite uncertain. A small Ω should reveal itself by a break after a few days in the afterglow light curve. A break is indeed observed in a few cases such as GRB 990510 (Harrison et al. 1999) where $\frac{\Omega}{4\pi}$ could be as small as 0.01. However, most afterglows do not show any break which means that Ω is usually not very small ($\frac{\Omega}{4\pi} \sim 0.1$?).

The source of cosmic GRBs must therefore be able to release a huge energy in a very short time. Possible candidates include the coalescence of two neutron stars (Eichler et al. 1989; Paczyński 1991), the disruption of the neutron star in a neutron star – black hole binary (Narayan et al. 1992; Mochkovitch et al. 1993) or the collapse of a massive star (Woosley 1993, Paczyński 1998). In all these cases the resulting configuration is expected to be a stellar mass black hole surrounded by a thick disc. Since the power emitted by GRBs is orders of magnitude larger than the Eddington limit it cannot be radiated by a static photosphere. The released energy generates a fireball which then leads to the formation of a wind. Moreover, this wind has to become highly relativistic in order to avoid the compactness problem and produce gamma-rays (Baring 1995; Sari & Piran 1997). Values of the Lorentz factor as high as $\Gamma = 100$ – 1000 are required, which limits the allowed amount of baryonic pollution to a remarkably low level. Only a few mechanisms have been proposed to produce a wind under such severe constraints : (i) magnetically driven outflow originating from the disc or powered by the Blandford–Znajek (1977) process (Thomson 1994; Mészáros & Rees 1997; Daigne & Mochkovitch 1999; Lee et al. 1999) ; (ii) reconnection of magnetic field lines in the disc corona (Narayan et al. 1992) ; (iii) neutrino–antineutrino annihilation in a funnel along the rotation axis of the system (Mészáros & Rees 1992; Mochkovitch et al. 1993, 1995). Mechanisms (i) and (ii) require that the magnetic field in the disc reaches very high values $B \gtrsim 10^{15}$ G. Our preliminary study (Daigne & Mochkovitch 1999) of the wind emitted from the disc shows that it can avoid baryonic pollution only if some very severe constraints on the dissipation in the disc and the field geometry are satisfied. Some recent works (Ruffert et al. 1997) have also shown that mechanism (iii)

* Present address: Max-Planck-Institut für Astrophysik, Karl-Schwarzschild-Str. 1, D-85740 Garching bei München, Germany

is probably not efficient enough to power a gamma-ray burst, except may be for the shortest events.

When the wind has reached its terminal Lorentz factor, the energy is mainly stored in kinetic form and has to be converted back into gamma-rays. Two main ideas have been proposed to realize this conversion. The first one is the so-called external shock model (Rees & Mészáros 1992; Mészáros & Rees 1993). The wind is decelerated by the external medium, leading to a shock. Gamma-rays are emitted by the accelerated electrons in the shocked material through the synchrotron and/or inverse Compton mechanisms. This model has been studied in details (Fenimore et al. 1997; Panaitescu et al. 1997; Panaitescu & Mészáros 1998) and seems unable to reproduce some important features of GRBs such as their strong temporal variability (see however Dermer & Mitman 1999). Conversely, the external shock model reproduces very well the delayed emission at lower energy from the afterglows (Mészáros & Rees 1997; Wijers et al. 1997).

The second proposal is the internal shock model (Rees & Mészáros 1994) where the wind is supposed to be formed initially with a very inhomogeneous distribution of the Lorentz factor. Rapid parts of the wind then catch up with slower ones leading to internal shocks where gamma-rays are again produced by synchrotron or inverse Compton radiation. We have started a study of this model in a previous paper (Daigne & Mochkovitch 1998, hereafter DM98) where the wind was simply made of a collection of “solid” shells interacting by direct collisions only (all pressure waves were suppressed). The very encouraging results we obtained had to be confirmed by a more detailed study. We have therefore developed a relativistic hydrocode to follow the evolution of the wind. We present the code and the main results in this paper. We write in Sect. 2 the lagrangian equations of hydrodynamics in special relativity. In Sect. 3 we describe the numerical method we use to solve them and we present the tests we performed to validate the method. We display our results in Sect. 4 and Sect. 5 is the conclusion.

2. Lagrangian equations of hydrodynamics in special relativity

We write in a fixed frame the equations of mass, momentum and energy conservation in spherical symmetry :

$$\frac{\partial V_m}{\partial t} - \frac{\partial (R^2 v)}{\partial m} = 0, \tag{1}$$

$$\frac{\partial S_m}{\partial t} + R^2 \frac{\partial P}{\partial m} = 0, \tag{2}$$

$$\frac{\partial E_m}{\partial t} + \frac{\partial (R^2 P v)}{\partial m} = 0, \tag{3}$$

where R and t are respectively the spatial and temporal coordinates in the fixed frame. The following quantities

appear in Eqs. 1–3 : P is the pressure in the fluid local rest frame, v is the fluid velocity in the fixed frame and V_m , S_m and E_m are the specific volume, momentum density and energy density (including mass energy) in the fixed frame. These three quantities are related to quantities in the fluid local rest frame :

$$V_m = \frac{1}{\rho \Gamma}, \tag{4}$$

$$S_m = h \Gamma v, \tag{5}$$

$$E_m = h \Gamma - \frac{1}{\Gamma} \frac{P}{\rho}, \tag{6}$$

where $\Gamma = \frac{1}{\sqrt{1-v^2}}$ is the Lorentz factor, ρ is the rest-mass density and $h = 1 + \epsilon + \frac{P}{\rho}$ is the specific enthalpy density (ϵ being the specific internal energy density). The lagrangian mass coordinate m is defined by

$$m = \int_{R_{\min}}^R \frac{R^2}{V_m} dR, \tag{7}$$

R_{\min} being the radius of the back edge of the wind. The system of Eqs 1–3 is completed by the equation of state

$$P = (\gamma - 1) \rho \epsilon, \tag{8}$$

the adiabatic index γ being a constant.

In the non-relativistic limit ($v \rightarrow 0$ and $h \rightarrow 1$), the quantities V_m , S_m and E_m become equal to their newtonian counterparts $\frac{1}{\rho}$, v and $E = 1 + \epsilon + \frac{v^2}{2}$ and Eqs. 1–3 then reduce to the classical equations of lagrangian hydrodynamics in spherical symmetry. The great similarity between the relativistic and classical equations will allow us to use the powerful numerical methods which have been developed in classical hydrodynamics to follow the evolution of a fluid with shocks.

3. Numerical method

3.1. Extension of the PPM to 1D lagrangian relativistic hydrodynamics in spherical symmetry

An extension of the Piecewise Parabolic Method of Colella and Woodward (1984) to 1D eulerian relativistic hydrodynamics in planar symmetry has been already presented by Martí and Müller (1996). We follow exactly the same procedure to extend the PPM to the lagrangian case in spherical symmetry.

We adopt $W = (V_m, S_m, E_m)$ as the set of variables. If the mass-averaged values W_j^n of W at time t^n in each cell $[m_{j-\frac{1}{2}}, m_{j+\frac{1}{2}}]$ extending from $R_{j-\frac{1}{2}}^n$ to $R_{j+\frac{1}{2}}^n$ are known, the values W_j^{n+1} at time $t^{n+1} = t^n + \Delta t$ are computed in four steps:

a) Reconstruction step

The variables $U = \left(\frac{1}{\rho}, P, v\right)$ are obtained from W in each cell by solving the following equation in h :

$$h^2 + (\gamma - 1) h - \gamma E_m \sqrt{S_m^2 + h^2} + \gamma S_m^2 = 0. \tag{9}$$

Once h is known, the other quantities are easily computed since $v = \frac{S_m}{\sqrt{S_m^2 + h^2}}$ and $\frac{1}{\rho} = \Gamma V_m$. These mass-averaged values are then interpolated by polynomials in the way described in the original paper by Colella and Woodward (1984). We use the same modifications of the coefficients of the interpolation polynomials, leading to a steeper representation of discontinuities and a monotone representation of smoother parts.

b) Effective states

At each interface $j + \frac{1}{2}$, two effective states $U_{j+\frac{1}{2},L}$ and $U_{j+\frac{1}{2},R}$ (L and R denote the left and right sides of the interface) are constructed by mass-averaging these quantities in the region of cells j and $j + 1$ connected to the interface $j + \frac{1}{2}$ by a characteristic line during the time step.

c) Riemann solver

At each interface $j + \frac{1}{2}$, the two effective states $U_{j+\frac{1}{2},L}$ and $U_{j+\frac{1}{2},R}$ define a Riemann problem (two constant states separated by a discontinuity surface), which is known to give rise, like in newtonian hydrodynamics, to two new states $U_{j+\frac{1}{2},L*}$ and $U_{j+\frac{1}{2},R*}$ separated by a contact discontinuity and related to the initial states $U_{j+\frac{1}{2},L}$ and $U_{j+\frac{1}{2},R}$ either by a shock or a rarefaction wave. The common values of the pressure and the velocity of the two new intermediate states are given by the implicit equation

$$v_* = v_{L*}(p_*) = v_{R*}(p_*) . \quad (10)$$

An analytic expression (for a polytropic gas) of

$$v_{S*}(p) = \begin{cases} \mathcal{R}_S(p) & \text{if } p \leq p_S \text{ (rarefaction wave)} \\ \mathcal{S}_S(p) & \text{if } p \geq p_S \text{ (shock wave)} \end{cases} \quad (11)$$

(where S either refers to the L or R state) has been worked out by Martí and Müller (1994). Equation (11) is solved using Brent's method to obtain the pressure p_* and the velocity v_* of the intermediate states at each interface.

d) Time advancement

The quantities W_j^n are calculated with numerical fluxes at each interface obtained from p_* and v_* in the same way than Colella and Woodward (1984).

3.2. Numerical tests

3.2.1. Relativistic shock tube

We have successfully checked our code against two usual tests in relativistic hydrodynamics. The first one is the shock tube problem which is simply a Riemann problem in which the initial states are at rest. We present in Fig.1 the results for $\rho_L = 1$, $p_L = 1000$, $v_L = 0$ and $\rho_R = 1$, $p_R = 0.1$, $v_R = 0$. The adiabatic index is $\gamma = \frac{5}{3}$ and the discontinuity is initially located at $x = 0.5$. The figure is plotted at a time $t = 0.303$ for a grid of 1000 zones initially equally spaced. The agreement between the exact and numerical profiles is satisfactory. The positions of the contact discontinuity and the shock are very accurate. The

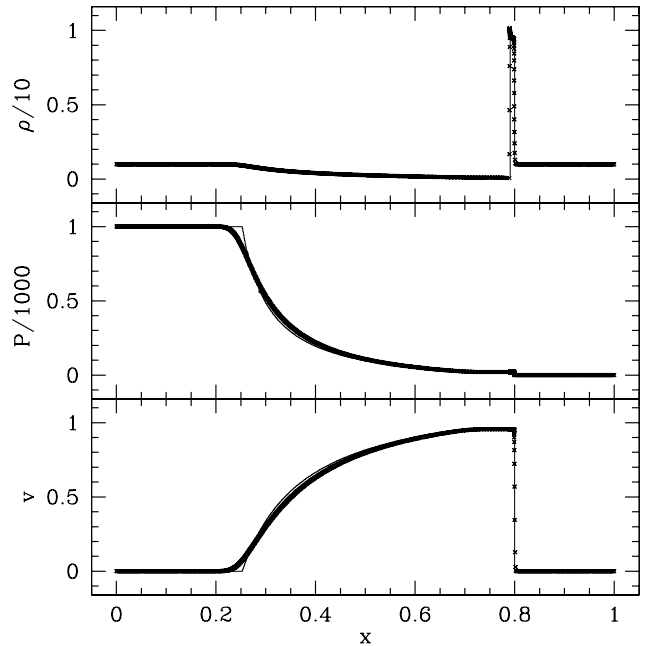


Fig. 1. Relativistic shock tube problem with $\rho_L = 1$, $p_L = 1000$ and $\rho_R = 1$, $p_R = 0.1$: Exact (solid line) and numerical profiles of density, pressure and velocity at $t = 0.303$.

density, pressure and velocity of the post-shock state are also exact. However, the value of the density in the immediate vicinity of the contact discontinuity shows a small non-physical increase, which is more pronounced when the shock is stronger and disappears when the shock is weak (as in the shock tube problem with $\rho_L = 10$, $p_L = 13.3$ and $\rho_R = 1$, $p_R = 0$, which has been considered by several authors). In the context of the internal shock model for GRBs, the shocks are only mildly relativistic and we do not observe any unexpected increase of the density in the results presented below.

3.2.2. Spherical shock heating

This test consists in a cold fluid, which is initially homogeneous ($\rho(R, 0) = \rho_0$) and enters a sphere of radius 1 at constant velocity v_0 . The fluid bounces at $R = 0$ and is heated up. We present in Fig.2 the results for $\rho_0 = 1$, $p_0 = 10^{-6}$ and $v_0 = -0.99999$ at $t = 1.90$. The adiabatic index is $\gamma = \frac{4}{3}$ and we used a grid of 1000 zones initially equally spaced. In the considered case of a cold homogeneous fluid, an analytical solution is known. The shocked state is at rest with a density $\rho'_0 = \frac{1}{\Gamma_0^2} \left(\frac{\gamma \Gamma_0 + 1}{\gamma - 1} \right)^3 \rho_0$ and a pressure $p'_0 = (\gamma - 1)(\Gamma_0 - 1)\rho'_0$. At time t the unshocked cold fluid of velocity v_0 has a distribution of density $\rho(R, t) = \rho_0 \left(1 + \frac{|v_0|t}{R} \right)^2$. The numerical profiles appear accurate except in the vicinity of the origin. The shock propagates with the correct velocity and the post-shock values of density and pressure are well reproduced.

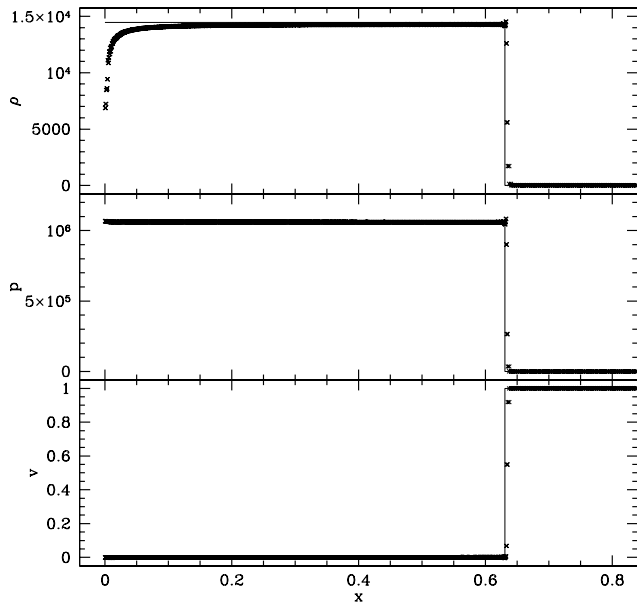


Fig. 2. Spherical shock heating : Exact (solid line) and numerical profiles of density, pressure and velocity at $t = 1.90$.

We therefore conclude that the treatment of the geometrical terms in Eqs 1–3 is correct. We have not tried to improve the computation near the center, which is not of major importance in the context of the internal shock model for GRBs where most of the emission takes place far from the origin.

4. Results and discussion

We have used our code to follow the evolution of a relativistic wind with a very inhomogeneous initial distribution of the Lorentz factor. The first results have been already presented for small values of the Lorentz factor $\Gamma \sim 40$ (Daigne & Mochkovitch 1997). Here we describe our results for the large Lorentz factors ($\Gamma \geq 100$) which are relevant for the study of GRBs. We first consider the case of a simple single-pulse burst.

4.1. Initial state

Whatever the initial event leading to a GRB may be (NS–NS or NS–BH merger, “hypernova”, etc), the system at the end of this preliminary stage is probably made of a stellar mass black hole surrounded by a thick disc (the “debris” torus). We consider that E , a substantial fraction of the available energy of the system, is injected at a typical radius R_0 into a wind emitted during a duration t_W with a mass flow \dot{M} . We do not discuss here the physical processes controlling \dot{M} , t_W and E but we assume that the baryonic load $\frac{1}{\eta} = \frac{\dot{M}t_W c^2}{E}$ is very small.

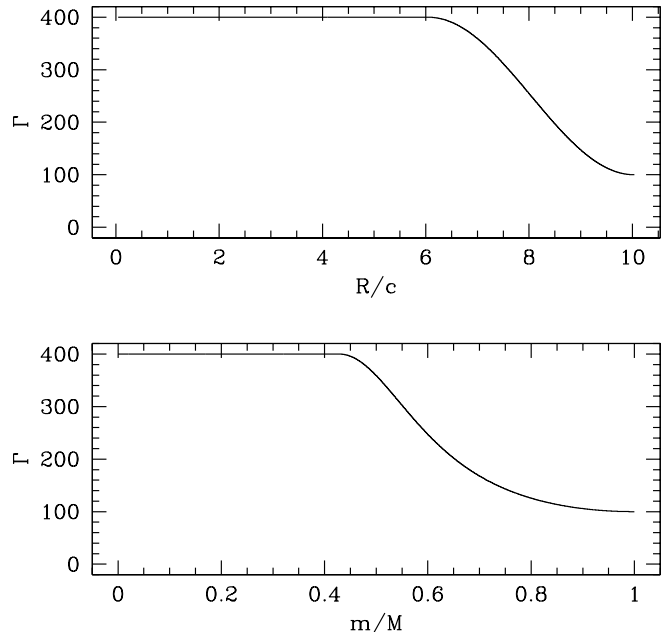


Fig. 3. Initial state at $t = 10$ s for $t_W = 10$ s. An energy $E = 2 \cdot 10^{52} / 4\pi$ erg/sr has been injected into the wind, whose mass is $7.76 \cdot 10^{28}$ g (which corresponds to an average Lorentz factor $\bar{\Gamma} \sim 290$). The masses of the fast ($\Gamma = 400$) and “slow” parts ($\Gamma = 100 \rightarrow 400$) are equal. Upper panel : eulerian distribution of the Lorentz factor in the wind. Lower panel : corresponding lagrangian distribution.

The wind converts its internal energy into kinetic energy during its free expansion in the vacuum (the effect of the interstellar medium is negligible at this early stage) and accelerates until it reaches a Lorentz factor $\Gamma \simeq \eta$ at a typical radius ΓR_0 (Mészáros et al. 1993). This is where our simulation starts.

More precisely, we define our initial state as follows. We consider that from $t = 0$ to $t = t_W$, a wind with a distribution of the Lorentz factor defined by

$$\Gamma(t) = \begin{cases} 250 - 150 \cos\left(\pi \frac{t}{0.4 t_W}\right) & \text{if } t \leq 0.4 t_W \\ 400 & \text{if } t \geq 0.4 t_W \end{cases} \quad (12)$$

has been produced by the source and that its back edge has reached $R_{\min} = 400 R_0 = 1.2 \cdot 10^4$ km (we adopt $R_0 = 30$ km). We suppose that energy is injected at a constant rate \dot{E} (we adopt $\dot{E} = \frac{2 \cdot 10^{51}}{4\pi}$ erg.s⁻¹/sr in the following), so that the total energy injected into the wind simply equals $E = \dot{E} t_W$ and the injected mass flux is $\dot{M}(t) = \frac{\dot{E}}{\Gamma(t) c^2}$. The density profile in this initial state can be calculated if we assume that the internal energy is very small compared to the kinetic energy, which is indeed the case when the wind has reached its terminal Lorentz factor ($\frac{P}{\rho c^2} \ll 1$). The eulerian and lagrangian profiles of Γ in the wind at $t = t_W$ are shown in Fig.3 for $t_W = 10$ s

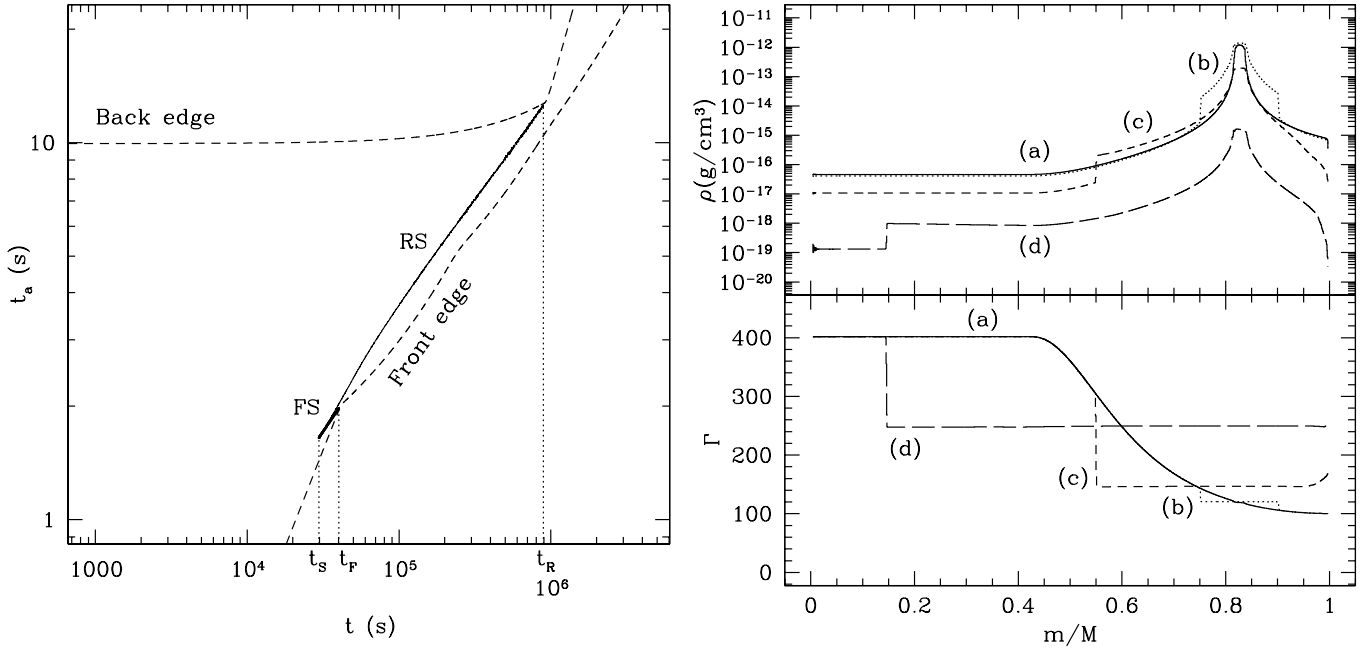


Fig. 4. *Left panel* : Paths of the back and front edges and of the forward and reverse shocks in the $t-t_a$ plane. The two shocks appear at t_S , the forward shock reaches the front edge very soon at t_F and the reverse shock reaches the back edge later at t_R . *Right panel* : Distribution of density ρ and Lorentz factor Γ at different times: (a) $t = 2.5 \cdot 10^4$ s, just before the formation of the two shocks; (b) $t = 3.0 \cdot 10^4$ s: the two shocks are clearly visible; (c) $t = 3.1 \cdot 10^4$ s: the forward shock has just reached the front edge. The reverse shock has still more than one half of the mass to sweep; (d) $t = 5.6 \cdot 10^5$ s: just before the reverse shock reaches the back edge.

and $E = \frac{2 \cdot 10^{52}}{4\pi}$ erg/sr. We have adopted $\frac{P}{\rho c^2} = 10^{-3}$ and have checked that the results do not depend on this small value.

4.2. Dynamical evolution

The fast part of the wind catches up with the slower one. The matter is strongly compressed in the collision region, the velocity gradient becomes very steep and at $t_S \sim 3 \cdot 10^3 t_W$, two shocks appear: a forward shock reaching the front edge at $t_F \sim 4 \cdot 10^3 t_W$ and a reverse shock reaching the back edge at $t_R \sim 9 \cdot 10^4 t_W$. The hot and dense matter behind these two internal shocks radiates and produces the observed burst. The radiation losses are not taken into account in the dynamics, which is probably not a too severe approximation since the dissipated energy represents about 10% of the total kinetic energy of the wind.

When the two shocks have reached the edges, the evolution becomes unimportant regarding the emission of gamma-rays: two rarefaction waves develop at each edge and the wind continues to expand and cool. In fact, at this stage, the interstellar medium should absolutely be included in the calculation. An external shock propagates into the ISM which produces the afterglow and a reverse shock crosses the wind which can also lead to an observ-

able emission. All these effects are not included in the present simulation, which is stopped when the two internal shocks have reached the wind edges.

We present in Fig.4 (left panel) the paths in a $t-t_a$ plot ($t_a = t - \frac{R}{c}$ is the arrival time of photons emitted at time $t_e = t$ on the line of sight at a distance R from the source) of the two shocks and of the two edges of the wind. In the right panel the corresponding distributions of Γ and ρ are plotted at different times.

4.3. Gamma-ray emission and properties of the observed burst

4.3.1. Method of calculation

Consider an internal shock located at a distance $R = R_e$ from the source at a time $t = t_e$ in the fixed frame. The density $\rho_{*,S}$, the Lorentz factor $\Gamma_{*,S}$ and the specific internal energy $\epsilon_{*,S}$ of the shocked (*) and unshocked (S) material are known from our hydrodynamical simulation. This shock will produce a contribution to the GRB which will be observed at an arrival time

$$t_a = t_e - \frac{R_e}{c} \quad (13)$$

and which will last

$$\Delta t_a = \frac{R_e}{2c\Gamma_r^2} \quad (14)$$

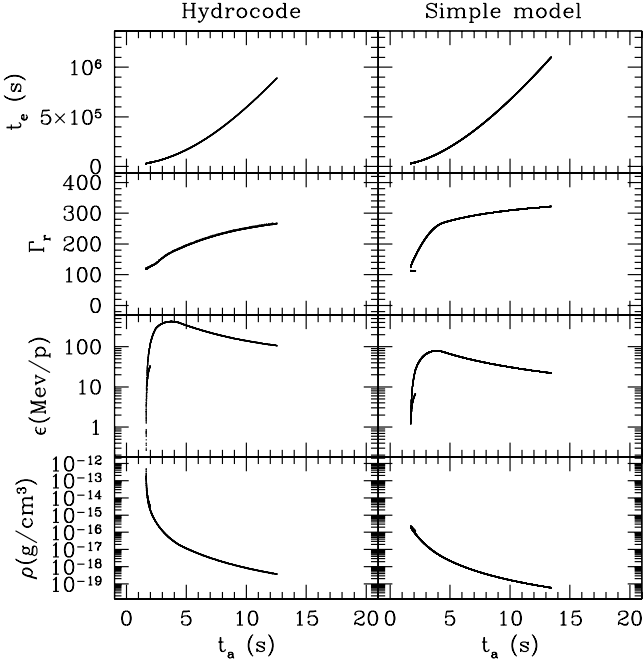


Fig. 5. *Single pulse burst (10s)* : Emission time t_e , Lorentz factor of the emitting material Γ_r , dissipated energy per proton ϵ_{diss} and density of the shocked material ρ as a function of arrival time t_a . Both contributions of the forward and reverse shocks are represented (the contribution of the forward shock is hardly visible).

where Γ_r is the Lorentz factor of the emitting material for which we adopt $\Gamma_r = \Gamma_*$. The luminosity of the shock is estimated by

$$L_{sh} = \dot{M}_{sh} \Gamma_* (\epsilon_* - \epsilon_S) \quad (15)$$

where \dot{M}_{sh} is the mass flux across the shock and $\epsilon_{diss} = \epsilon_* - \epsilon_S$ is the dissipated energy per unit mass in the frame of the shocked material.

Our code detects all the internal shocks present in the wind at a given time and saves their parameters in order to sum all the contributions to the emission and produce a synthetic gamma-ray burst. In a recent paper (DM98) we presented a simple model where the wind was idealized by a collection of “solid” shells interacting by direct collision only (i.e. all pressure waves were neglected). We detailed in this previous paper our assumptions to treat the emission of a given shock. We adopt here the same assumptions. The magnetic field in the shocked material is supposed to reach equipartition values

$$B_{eq} = \sqrt{\alpha_B 8\pi\rho\epsilon_{diss}} \quad (16)$$

with $\alpha_B = \frac{1}{3}$. The Lorentz factor of the accelerated electrons is calculated using the expression given by Bykov & Mészáros (1996) who consider the scattering of electrons by turbulent magnetic field fluctuations :

$$\Gamma_e = \left[\frac{\alpha_M m_p \epsilon_{diss}}{\zeta m_e c^2} \right]^{1/(3-\mu)} \quad (17)$$

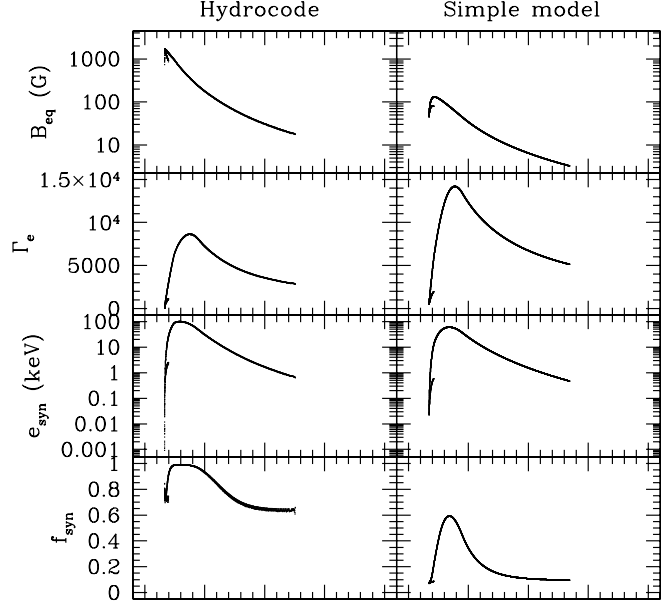


Fig. 6. *Single pulse burst (10s)* : Magnetic field B_{eq} , Lorentz factor of the accelerated electrons Γ_e , synchrotron energy e_{syn} and fraction of the energy which is radiated by the synchrotron process f_{syn} as a function of arrival time t_a . Both contributions of the forward and reverse shocks are represented (the contribution of the forward shock is hardly visible).

where $\alpha_M = 0.1 - 1$ is the fraction of the dissipated energy which goes into the magnetic fluctuations; ζ is the fraction of the electrons which are accelerated and μ ($1.5 \leq \mu \leq 2$) is the index of the fluctuation spectrum. For $\zeta \sim 1$ and $\mu = 2$, Eq. (17) corresponds to the usual equipartition assumption, leading to Γ_e of a few hundreds. In this case, the emission of gamma-rays could result from inverse Compton scattering on synchrotron photons. Bykov and Mészáros however suggests that only a small fraction $\zeta \sim 10^{-3}$ of the electrons may be accelerated, leading to Γ_e values of several thousands. In this last case, synchrotron radiation can directly produce gamma-rays of typical energy

$$E_{syn} = 500 \frac{\Gamma_r B_{eq}}{300 1000 \text{ G}} \left(\frac{\Gamma_e}{10^4} \right)^2 \text{ keV} \quad (18)$$

We now present a detailed comparison of the results of our hydrodynamical code with those previously obtained with the simple model (DM98) for a single pulse burst. We have plotted in Fig. 5 the values of t_e , Γ , ϵ_{diss} and ρ as function of t_a for the forward and reverse shocks. We observe an overall similarity between the two calculations, despite the crude approximations of the simple model. Not surprisingly, the worst estimated quantities are the post-shock density and the dissipated energy per proton, which are underestimated by a factor of ~ 5 . Conversely, the

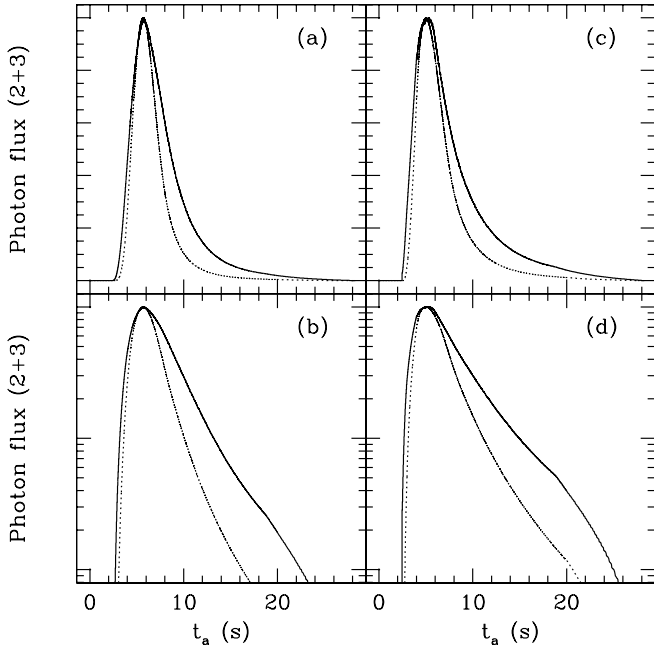


Fig. 7. Burst profiles for the initial distribution of the Lorentz factor shown in Fig. 3. The photon flux (normalized to the maximum count rate) is given in the interval 50 – 300 keV, corresponding to BATSE bands 2+3. (a) Profile obtained with the expression of Γ_e given by Eq. (17); (b) same as (a) in logarithmic scale, which illustrates the exponential decay after maximum; (c) profile obtained with a constant Γ_e ; (d) same as (c) in logarithmic scale. In the four panels, the full line represents the profile obtained with the hydrocode while the dashed line corresponds to the simple model.

emission time and the Lorentz factor of the emitting material are correctly reproduced. The emission starts earlier in the simple model where there is no preliminary phase of compression before the formation of shocks (this leads to a larger underestimate of the density at the very beginning of the simulation), and ends later. The total efficiency of the dissipation process is also smaller $\sim 5\%$ instead of 12% for the detailed model.

The other quantities B_{eq} , Γ_e and e_{syn} are not directly given by the hydrodynamical simulation but are parametrized by α_B , α_M , ζ and μ , whose values are unknown. To make a useful comparison between the two series of results, we take the same α_B and μ in the two cases but adjust α_M/ζ so that the typical synchrotron energy is the same. The corresponding values of B_{eq} , Γ_e and e_{syn} are represented in Fig. 6 with $\alpha_B = 1/3$, $\mu = 1.75$ and $\alpha_M/\zeta = 100$ for the hydrocode and 1000 for the simple model. As expected because of the differences in density and dissipated energy, the magnetic field is underestimated by a factor of 5 in the simple model. This is corrected by our choice of parameters for Γ_e and the resulting synchrotron energies are very similar in the two

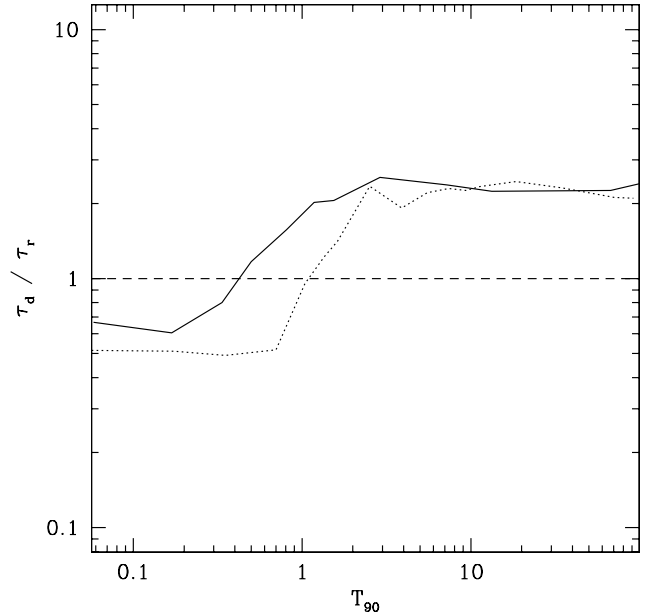


Fig. 8. Ratio of the decay to rise times as a function of burst duration. The initial distribution of the Lorentz factor is given by Eq. (12) and the total energy injected into the wind is proportional to t_W : $E = \frac{2 \cdot 10^{52}}{4\pi} \left(\frac{t_W}{10 \text{ s}}\right)$ erg/sr. The full line corresponds to the results of the hydrocode while the dashed line shows the same relation obtained with the simple model.

cases. Also notice that the efficiency of the synchrotron process is smaller in the simple model due to a poor estimate of the mass flux across the shock.

The agreement between the two calculations is satisfactory and allows to be quite confident in the results of the simple model. Compared to the hydrodynamical code, the simple model has very short computing times and enables a detailed exploration of the temporal and spectral properties of synthetic bursts which was presented in our previous paper (DM98). We show in the next section the detailed results obtained with the hydrocode in the case of a single pulse burst.

4.3.2. Temporal properties

The contributions of the forward and the reverse shocks are added to construct the synthetic burst. We assume that the photons emitted from t to $t + dt$ by an internal shock of current luminosity L_{sh} are distributed according to a simple power-law spectrum

$$\frac{d(En(E))}{dE} \propto \frac{L_{sh} dt}{E_{syn}} \left(\frac{E}{E_{syn}}\right)^{-x}, \quad (19)$$

where we adopt $x = 2/3$ or $x = 3/2$ (the two extreme low energy index that are expected for a synchrotron spectrum) for $E < E_{syn}$ and $2 < x < 3$ for $E > E_{syn}$ ($x = 2.5$

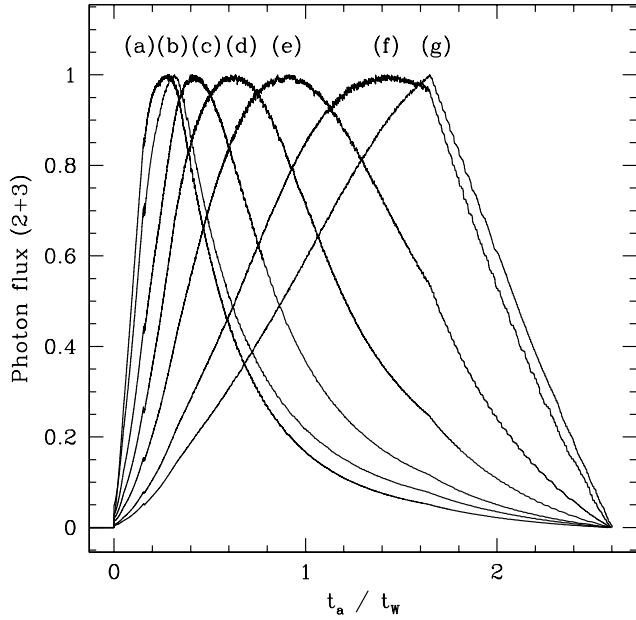


Fig. 9. Evolution of the profiles with duration. The initial distribution of the Lorentz factor is given by Eq. (12) and the total injected energy is $E = \frac{2}{4\pi} \frac{10^{52}}{\left(\frac{t_w}{10 \text{ s}}\right)}$ erg/sr. The different profiles correspond to (a) $t_w = 10 \text{ s}$; (b) $t_w = 5 \text{ s}$; (c) $t_w = 2 \text{ s}$; (d) $t_w = 1 \text{ s}$; (e) $t_w = 0.5 \text{ s}$; (f) $t_w = 0.2 \text{ s}$; (g) $t_w = 0.1 \text{ s}$.

in the following). We take into account cosmological effects (time dilation and redshift) assuming that the burst is located at $z = 0.5$.

We have plotted in Fig.7a the photon flux observed in BATSE bands 2+3 for the initial distribution of Lorentz factor shown in Fig.3, calculated either with the hydrocode (with $\frac{\alpha M}{\zeta} = 100$) or the simple model (with $\frac{\alpha M}{\zeta} = 1000$). The two profiles look similar but the hydrodynamical code leads to a slower decay. With t_5 (resp. t_{95}) being the time when 5% (resp. 95 %) of the total fluence has been received, we obtain a duration $T_{90} = t_{95} - t_5 = 10.4 \text{ s}$ instead of 6.67 s with the simple model. Figure 7b illustrates that the exponential decay of the burst is also nicely reproduced with the detailed calculation. However, if we define t_{max} as the time of maximum count rate and $\tau_r = t_{max} - t_5$ and $\tau_d = t_{95} - t_{max}$ as the rise and the decay times, we get a ratio $\tau_d/\tau_r = 2.08$. DM98 found that a larger value of τ_d/τ_r and a corresponding profile closer to the characteristic “fast rise – exponential decay” (FRED) shape is obtained by assuming that the fraction ζ of accelerated electrons increases with the dissipated energy per proton ϵ_{diss} . As in DM98 we adopt $\zeta \propto \epsilon_{diss}$, so that Γ_e is independent of ϵ_{diss} . Figures 7c and 7d show the resulting profiles with $\Gamma_e = 5000$ for the hydrocode and $\Gamma_e = 10000$ for the simple model. The profile then better reproduces a typical FRED shape.

The observed tendency of short bursts to become symmetric (Norris et al. 1996) has been tested in DM98 with

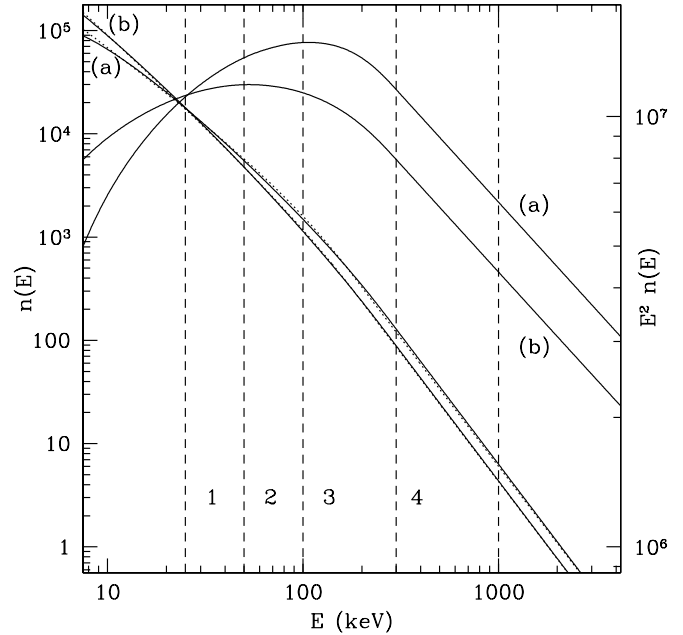


Fig. 10. Spectrum of the burst presented in figure 9(c) ($t_w = 2 \text{ s}$). The number of photons per energy interval $n(E)$ and the product $E^2 n(E)$ are shown in arbitrary unit. This product is maximum at peak energy $E_p = 403 \text{ keV}$ in case (a) ($x = -2/3$) and $E_p = 193 \text{ keV}$ in case (b) ($x = -3/2$). The dashed lines show a fit of each spectrum with Band’s formula in the interval 10 keV – 10 MeV (parameters are given in the text).

the simple model. The basic behaviour was reproduced but the effect was even exaggerated since, for $T_{90} < 1 \text{ s}$, τ_d/τ_r was smaller than unity i.e. the decline was faster than the rise. As can be seen in Fig. 8 and 9, the situation is improved with the hydrocode since now $\tau_d/\tau_r \sim 1$ for $T_{90} \sim 0.4 \text{ s}$. However, the shortest bursts are still asymmetric with $\tau_d/\tau_r \sim 0.6$ for $T_{90} \leq 0.2 \text{ s}$.

Figure 8 also shows that the ratio τ_d/τ_r is limited to a maximum value of ~ 2.5 for the longest bursts which appears to be in contradiction with the short rise times observed in some cases. As discussed in DM98, an initial distribution of the Lorentz factor with a steeper gradient than the one used here (Eq. (12)) can indeed increase τ_d/τ_r but extreme values (such as τ_d/τ_r possibly larger than 10 in GRB 970208) might still be difficult to reproduce.

4.3.3. Spectral properties

In DM98 we presented a complete study of the global and instantaneous spectral properties of synthetic bursts calculated with the simple model. Since these spectral properties are hardly different when calculated with the hydrocode, we do not present them in detail again. We just show in Fig. 10 the shape of the global spectrum calculated for the single pulse burst. Despite the very simple

form adopted for the instantaneous spectrum (Eq. 19), the sum of all the elementary contributions produces an overall spectrum with a more complex shape, which is well reproduced with Band’s formula (Band et al. 1993)

$$n(E) = A \left(\frac{E}{100 \text{ keV}} \right)^\alpha \exp \left(-\frac{E}{E_0} \right) \text{ for } E \leq (\alpha - \beta)E_0$$

$$n(E) = A \left[\frac{(\alpha - \beta)E_0}{100 \text{ keV}} \right]^{\alpha - \beta} \exp(\alpha - \beta) \left(\frac{E}{100 \text{ keV}} \right)^\beta$$

for $E \geq (\alpha - \beta)E_0$. (20)

We find values of the parameters comparable to those observed in real bursts. The best fits in Fig. 10 correspond to $\alpha = -0.935$, $\beta = -2.42$ and $E_0 = 239$ keV in case (a) ($x = -2/3$) and $\alpha = -1.60$, $\beta = -2.47$ and $E_0 = 609$ keV in case (b) ($x = -3/2$). As x is limited to the range $2/3 < x < 3/2$, we cannot get spectra with low energy slopes flatter than $-2/3$ as they are observed in several bursts (Preece et al. 2000). A more detailed description of the radiative processes is then needed to reproduce these extreme slopes (an attempt to solve this problem is proposed by Meszaros & Rees 2000).

However, even with the crude modelization of the instantaneous spectra which is used here, it has been shown in DM98 that several spectral properties of GRBs are reproduced. In particular, the hard to soft evolution during a pulse and the change of pulse shape as a function of energy as well as the duration – hardness ratio relation which appears as a natural consequence of the internal shock model. These important spectral features are confirmed in our detailed hydrodynamical calculation.

4.4. Case of more complex bursts

An important property of the internal shock model is its ability to produce a great variety of temporal profiles. Norris et al. (1996) have shown that complex bursts can generally be analysed in terms of a series of (possibly overlapping) simple pulses. This result is readily interpreted in the context of the internal shock model. A wind made of a succession of fast and slow shells will produce a succession of pulses which will add to form a complex burst.

We present such examples of complex bursts in Fig. 11 and 12. The first one (Fig. 11) is produced by an initial distribution of the Lorentz factor made of five consecutive identical patterns. Each pattern made of a slow and a rapid part produces its own individual pulse and the resulting burst has a complex shape with five, very similar, pulses. Our second example (Fig. 12) uses the same type of initial distribution of the Lorentz factor but the slow parts now have non equal Γ values. The resulting burst is more realistic with four pulses of different intensities.

We did not treat with the hydrocode a large number of cases as we did with the simple model. Nevertheless we confirmed the essential result that the variability introduced in the initial distribution of the Lorentz factor

is present in the burst profile with the same time scale. The profile therefore appears as a direct indicator of the activity of the central engine.

5. Conclusions

This paper is the continuation of our study of the internal shock model started in DM98. We developed a 1D lagrangian relativistic hydrocode (in spherical symmetry) to validate our previous simpler approach where all pressure waves were neglected in the wind. Our code is an extension of the classical *PPM* method of Colella and Woodward (1984) in the spirit of the work by Martí & Müller (1996) for the eulerian case in planar symmetry.

A detailed comparison has been made between the hydrocode and the simple model in the case of a single pulse burst. It appears that the dynamical evolution of the wind is well reproduced by the simple model, which is not too surprising because the wind energy is largely dominated by the kinetic part so that the effect of pressure waves is small. Only one physical quantity – the density of the shocked material – is strongly underestimated in the simple model. In order to make valuable comparisons between the two calculations we have therefore adjusted the equipartition parameters so that the mean value of the synchrotron energy is the same in the two cases. The synthetic bursts which are then obtained are very similar which proves that our first approach was essentially correct and confirm our previous results. A similar conclusion was reached by Panaitescu and Mészáros (1999) who performed a comparable study.

The internal shock model can easily explain the great temporal variability observed in GRBs. The main characteristic features of individual pulses are well reproduced: (1) pulses have typical asymmetric “FRED” profiles; (2) the pulse width decreases with energy following a power-law $W(E) \propto E^{-p}$ with $p \sim 0.4$; (3) short pulses show a tendency to become more symmetric. Our model still gives very short pulses which decay faster than they rise but the hydrodynamical simulation improves the situation compared to the simple model. Spectral properties of GRBs are also well reproduced. We obtain synthetic spectra which can be nicely fitted with Band’s function with parameters comparable to those observed in real GRBs. The spectral hardness and the count rate are correlated during the evolution of a burst with the hardness usually preceding the count rate. As also pointed in DM98, the duration–hardness relation is a natural consequence of the internal shock model. These results are very encouraging and the main difficulty which remains is the low efficiency (about 10%) of the internal shock model. As long as the energetics of GRBs and the mechanism initially operating in the central engine are not precisely identified, we cannot say if this is a critical problem or not. We still believe that the internal shock model is at present the most con-

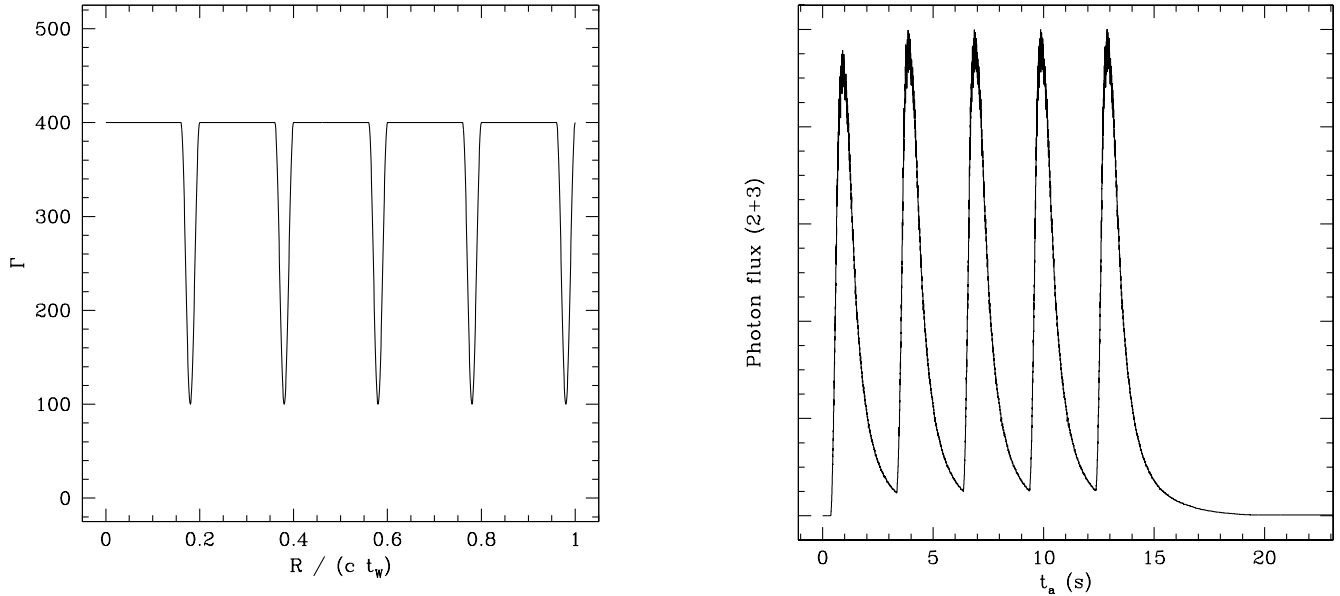


Fig. 11. Example of a complex burst. Left panel: initial distribution of the Lorentz factor with five identical patterns. Right panel: corresponding profile obtained with the hydrocode (normalized photon flux in the interval 50 - 300 keV). The wind is produced with a duration $t_W = 10$ s and the injected energy is $E = 10^{52}/4\pi$ erg/sr.

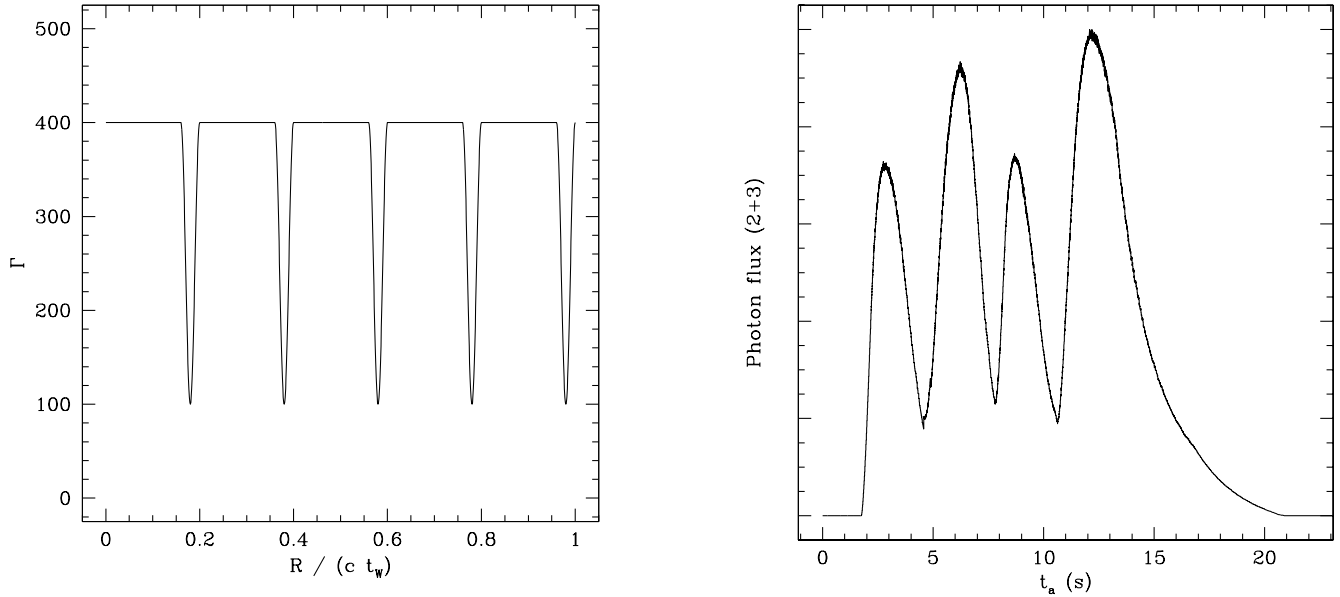


Fig. 12. Another complex burst. Left panel: initial distribution of the Lorentz factor with now four non identical patterns (Lorentz factors in the slow parts are different). Right panel: corresponding profile obtained with the hydrocode (normalized photon flux in the interval 50 - 300 keV). The wind is produced with a duration $t_W = 10$ s and the injected energy is $E = 10^{52}/4\pi$ erg/sr.

ving candidate to explain the gamma-ray emission from GRBs.

Next steps in this work will address the following questions. We first want to extend our hydrodynamical code to a non-adiabatic version in order to include the radiative losses in the dynamical calculation. We have already developed an “isothermal Riemann Solver” for that purpose

(Daigne & Mochkovitch 1997). We would also like to study the effects of the external medium, with a special attention to the reverse shock which propagates into the wind and possibly interacts with the internal shocks. Preliminary results with the simple method using “solid layers” have already been obtained (Daigne & Mochkovitch 1999) but they have to be confirmed by a hydrodynamical calcu-

lation. Finally, we would like to investigate the details of the emission process during internal shocks to solve some of the problems encountered by the synchrotron model.

Acknowledgements. We would like to thank the Departamento de Astronomía y Astrofísica de Valencia for their kind hospitality and acknowledge clarifying discussions with J.M. Martí and J.M. Ibáñez.

References

- Band D. et al., 1993, ApJ, 413, 281
 Baring M., 1995, ApSS, 231, 169
 Blandford R.D., Znajek R., 1977, MNRAS, 179, 433
 Bykov A., Mészáros P., 1996, ApJ, 461,L37
 Colella P., Woodward P.R., 1984, J. Comput. Phys. 54, 174
 Daigne F., Mochkovitch R., 1997, proceedings of the Fourth Huntsville Gamma-ray Burst Symposium
 Daigne F., Mochkovitch R., 1998, MNRAS, 296, 275 (DM98)
 Daigne F., Mochkovitch R., 1999, to appear in the proceedings of the 19th Texas Symposium, astro-ph 9907289
 Daigne F., Mochkovitch R., 1999, A&ASS, 138, 523
 Dermer C.D., Mitman K.E., 1999, ApJ, 513, L5
 Eichler D., Livio M., Piran T., Schramm D., 1989, Nat, 340, 126
 Fenimore E., Madras C., Nayakshin S., 1997, ApJ, 473, 998
 Fishman G.J., Meegan C.A., 1995, ARA&A, 33, 415
 Harrison F.A. et al., 1999, ApJ, 523, L21
 Lee H.K., Wijers R.A.M.J., Brown G.E., 1999, astro-ph 9906213
 Martí J.M. , Müller E., 1994, J. Fluid Mech. 258, 317
 Martí J.M. , Müller E., 1996, J. Comput. Phys. 123, 1
 Mészáros P., Laguna P., Rees M.J., 1993, ApJ 415, 181
 Mészáros P., Rees M.J., 1997, ApJ, 482, L29
 Mészáros P., Rees M.J., 1992, MNRAS, 257, 29
 Mészáros P., Rees M.J., 1993, ApJ, 405, 278
 Mészáros P., Rees M.J., 1997, ApJ, 476, 232
 Mészáros P., Rees M.J., 2000, ApJ, 530, 292
 Metzger M.R., Djorgovski S.G., Kulkarni S.R., Steidel C.C., Adelberger K.L., Frail D.A., Costa E., Frontera F., 1997, Nat, 387, 878
 Mochkovitch R., Hernanz M., Isern J., Martin X., 1993, Nat, 361, 236
 Mochkovitch R., Hernanz M., Isern J., Loiseau S., 1995, A&A, 293, 803
 Narayan R., Paczyński B., Piran T., 1992, ApJ, 395, L83
 Norris J., Nemiroff R., Bonell J., Scargle J., Kouveliotou C., Paciasas W., Meegan C., Fishmann G., 1996, ApJ, 459, 393
 Paczyński B., 1991, Acta Astron., 41, 257
 Paczyński B., 1998, ApJ, 494, L45
 Panaitescu A., Wen L., Laguna P., Mészáros P., 1997, ApJ, 482, 942
 Panaitescu A., Mészáros P., 1998, ApJ, 492, 683
 Panaitescu A., Mészáros P., 1999, ApJ, astro-ph 9808106
 Preece R.D., Briggs M.S., Malozzi R.S., Pendleton G.N., Paciasas W.S., Band D.L., 2000, ApJS, 126, 19
 Rees M.J., Mészáros P., 1992, MNRAS, 258, 41P
 Rees M.J., Mészáros P., 1994, ApJ, 430, L93
 Ruffert M., Janka H.T., Takahashi K., Schaeffer G., 1997, A&A, 319, 122
 Sari R., Piran T., 1997, MNRAS, 287, 110
 Thomson C., 1994, MNRAS, 270, 480
 van Paradijs J., et al., 1997, Nat, 386, 686
 Wijers R., Rees M.J., Mészáros P., 1997, MNRAS, 288, L51
 Woosley S.E., 1993, ApJ, 405, 273